Online-Journals.org

iJOE International Journal of Online and Biomedical Engineering

iJOE | eISSN: 2626-8493 | Vol. 21 No. 8 (2025) | OPEN ACCESS

https://doi.org/10.3991/ijoe.v21i08.55019

PAPER

A Novel 3D Method Based on Region-Growing and Morphology for Lung Segmentation

Hamza Halim[1](✉), Salma Hakim[1], Omar Boutkhoum[1], Mohamed Hanine[2], Abdelmajid El Moutaouakil[1]

[1]LAROSERI Laboratory, Department of Computer Science, Faculty of Sciences, Chouaib Doukkali University, El Jadida, Morocco

[2]LTI Laboratory, National School of Applied Sciences, Chouaib Doukkali University, El Jadida, Morocco

hamza.h@ucd.ac.ma

ABSTRACT

The purpose of this study is to help in the early detection of lung abnormalities by accurately segmenting the volume of interest from the CT scans. For this, we suggest a novel method that loads the volume by interpolating additional images to increase the resolution, thus improving the efficiency of the region-growing application, without any pre-processing, for segmenting voxels in the range of –1000 and –500 HU, and then applying a combination of chain code and region-growing to repair the lacunae due to blood vessels, trachea branches, and/or lesions that have intensities outside the range of interest. The validation of the segmentation result, using metrics, shows how close our method is to the ground truth, with an accuracy of 99.99%, a dice coefficient of 98.99%, an IoU of 98.02%, a recall of 98.44%, a precision of 99.56%, and an F1-score of 98.99%. Compared to UNET, UNET++, and 3D-UNET. Our method presents better results except for recall, which is higher than ours with a minor difference of 0.09–0.85%.

KEYWORDS

lung segmentation, interpolation, region-growing, morphology, UNET variants, medical image processing

1 INTRODUCTION

In 2022, the World Health Organization (WHO) claimed that lung cancer was in the second place with 2.21 million deaths [1]. However, the time taken to diagnose lung cancer has a direct influence on how it can be treated [2]. Early diagnosis and treatment, therefore, remain options for improving the chances of effectively treating lung lesions. But the first signs of lung damage are not necessarily visible, as they often appear small in the first stage. The use of 3D analysis contributes greatly to improving the accuracy of early diagnosis [3]. Currently, one of the most widespread imaging techniques is CT scanning [4], which can provide images distinct enough to establish a diagnosis. But to perform

Halim, H., Hakim, S., Boutkhoum, O., Hanine, M., Moutaouakil, A.E. (2025). A Novel 3D Method Based on Region-Growing and Morphology for Lung Segmentation. *International Journal of Online and Biomedical Engineering (iJOE)*, 21(8), pp. 171–190. https://doi.org/10.3991/ijoe.v21i08.55019

Article submitted 2025-02-18. Revision uploaded 2025-04-11. Final acceptance 2025-04-11.

this three-dimensional analysis, it is necessary to provide a 3D segmentation of the volume of interest.

In the field of medical image segmentation, a large number of scientific papers propose new methods or develop others, such as noise reduction methods [5], [6] and contrast enhancement [7], [8]. There are also semi-automatic and automatic segmentation approaches such as thresholding [9], [10], region-growing [11], [12], [13], and active contour [14], [15]. In recent years, we have started talking about artificial intelligence [16], [17], [18], mainly neural networks [19], [20], which have revolutionized image segmentation. LeNet-5 [21], AlexNet [22], GoogleNet [23], VGGNet [24], and DenseNet [25] are some of the neural models known for their efficiency in extracting discriminating features [26]. In 2015, O. Rennerberger and Brox [27] created the "U"-shaped convolutional neural network known as UNet. It is a connection-skipping encoder-decoder model. To improve predictions, the encoder reduces spatial dimensions and extracts features, the decoder progressively reconstructs spatial dimensions, and skipped connections enable low-level and high-level data to be combined. Since its creation, several variants of UNet have been developed to meet specific needs or to enhance its performance. These include 3D-UNET [28] for three-dimensional volumes, Attention-UNET [29], which introduces attention mechanisms to improve performance by focusing on important regions of the image, and ResUNet [30], which combines UNet with residual blocks to improve gradient propagation, and DenseUNet [31], which merges UNet with DenseNet for better feature reuse, NestedUNet (UNet++) [32] adds hierarchical connections between layers for finer-grained reconstruction. Recurrent Residual UNet (R2Unet) [33] combines recurrent and residual blocks in UNet. TransUNet [34] integrates Transformers with UNet to capture global relationships in images. UNet3+ [35] improves skip connections with multi-level aggregation mechanisms.

Given the anatomical shape of the trachea and parenchyma and their low intensity since the volume is largely filled with air, automatic segmentation of the respiratory system is a very difficult subject. In this paper, we propose a method that loads the volume by interpolating additional images to increase the resolution, thus improving the efficiency of the region-growing application for segmenting voxels in the –1000 and –500 HU range. A necessary separation process is applied if the lungs are connected before using a combination of chain code and region-growing to repair the lacunae due to blood vessels, trachea branches, and/or lesions that have intensities outside the range.

The rest of this paper is structured as follows: Section 2 presents the related work used to segment the organs of the respiratory system. Section 3 presents the datasets used and the details of the proposed method, followed by the results and discussions in Section 4, and finally, conclusions in Section 5.

2 RELATED WORKS

In this section, as shown in Table 1, we presented related works on image segmentation that were used to segment the lung, airway tree, and lung nodules in the rib cage. Liao et al. [36] focused on superpixels and self-generating neural forest techniques. As a first step, they utilized image characteristics to produce the sequences of ROI areas. To detect the superpixels, they then proposed a technique

for performing segmentation of the ROI on the image sequences using the Gradient and Sequential Linear Iterative Clustering Algorithm. After segmenting the lungs, they employed a self-generating neural forest (SGNF) that was modified for superpixel grouping by a genetic algorithm utilizing the gray and geometric details of the superpixels. Regarding the segmentation of the nodule, Cavalcanti et al. [37] pointed out the difficulties, for instance, that intensity-based methods are useful for the solitary nodules but not with the joined ones. Morphological methods, thresholding, and background estimation were employed, regarding the nodules as the foreground objects. Their method included the removal of the background and analyzing the slices without the nodules. They created a ResUNet model, which is a combination of UNet and ResNet34, and trained it with several datasets. To extract the lungs from the cross-section of CT scans, Nana He et al. [38] used SCN clustering made from Nystrom and GAC-based methods. An average ratio of overlapping of 0.9148 was obtained. In addition, to extract the lung on the sequences of the CT slices. Cha et al. [39] developed a new 4-D CT image segmentation technique that utilizes signed distance function and optical flow methods to exploit the inter-slice relationship. With a Bayesian approach to active contour modeling, Chung et al. [40] undertook the detection of juxta-pleural nodules. Which were incorporated by segmenting both new and old lung slices. To incorporate juxtapleural nodules into the lung region, Xiao et al. [41] apply modified convex hull, fractal geometry, and iterated thresholding techniques. Working with 97 private instances, they managed to achieve a pixel accuracy of 0.9245 and an IoU of 0.959. This paper [42] presents an airway segmentation technique for volumetric chest CT with the aid of a 2.5D CNN. It enhances the precision of volumetric CT image segmentation by employing 2.5D convolutional neural network approaches on three adjacent cuts processed in axial, sagittal, and coronal orientations. It was also tested on multilayer datasets, including the datasets of the EXACT'09 challenge, and achieved a Dice similarity coefficient of 0.8997 ± 0.0892. This paper [43] discusses the development of a semi-automated technique for lung nodules in CT scan slices that involves segmentation. The technique consists of two steps. Initially, a 2D ROI that carries a nodule is given to undertake patch-wise scanning along the axial direction using an adaptive ROI algorithm. Subsequently, the extracted VOI is scanned more thoroughly along the coronal and sagittal axes in patch-wise fashion using re-Us Netsi. The method achieved the average dice score of 87.5%. Suji et al. [44], [45] combine distance metric computation, chain coding, and morphological techniques to assess several slices one by one from a volume. Lung nodules were first segmented and then identified employing optical flow techniques. [46], [47]. Authors have been combining traditional graph cut methods with adaptive shape prior. Sousa et al. [48] achieved a dice coefficient of 0.9778 on the VESSEL12 dataset. Ma et al. [49] trained more than 40 models, including knowledge transfer, domain generalization, and small sample learning, using CT scans of COVID-19 patients. For the left and right lungs, they obtained mean dice coefficients of 0.973 and 0.977, respectively. Liu, W. et al. [50] improved the U-Net network by using the pre-training EfficientNet-b4 as the encoder and the residual block and LeakyReLU activation function in the decoder. While minimizing gradient instability caused by the multiplication impact of gradient backpropagation, the network can retrieve lung field properties efficiently. Gite et al. [51] used a UNet++ network for lung segmentation, achieving a mean IoU of 0.95 and a segmentation accuracy of 0.98.

Table 1. Summary of the respiratory system—lungs, airways, nodules—segmentation methods

Ref	Year	Network/Method	Advantages	Disadvantages	Dataset	Performance
[36]	2016	Gradient, sequential linear clustering	Demonstrates the value of utilizing the correlation between neighboring slices of the CT image series	Only private datasets are used for testing	LIDC-IDRI	Vof – 0.9222
[37]	2016	Background estimation by motion estimation methods	Results from segmentation are consistently achieved	No comparison with the benchmark dataset's state-of-the-art	LIDC-IDRI	Acc – 0.9913
[38]	2017	Active countour, spectral clustering	–	Introduction of key slice and slice similarity calculations	LIDC-IDRI	Vof – 0.9148
[39]	2018	Adaptive shape prior, motion, gaph-cut	–	Keeping the split item from combining with undesired surrounding tissue	LIDC-IDRI	Dsc – 0.68
[40]	2018	Bayesian	Exceeded the Chan-Vese model's performance.	Comparing the private dataset only with CV and NM-CV	LIDC-IDRI	Dsc – 0.9785
[41]	2018	Fractal Geometry, iterative thresholding	Reduced segmentation time	Only Japan was taken into account. The CAD pipeline was not used	LIDC-IDRI	IoU – 0.9245
[42]	2019	Deep Convolutional Neural Network	Complete segmentation model	–	LIDC-IDRI	Dsc – 0.6
[43]	2020	Deep Residual Unet	Better outcomes compared to state-of-the-art	Not every nodule in the dataset was used to assess performance.	LIDC-IDRI	Dsc – 0.875
[44]	2020	Morphology based	Better outcomes compared to state-of-the-art	Limited scans are employed in comparison.	LIDC-IDRI	Vof – 0.9859
[45]	2022	Morphology based				
[46]	2020	Morphology based	A new approach to integrating optical flow techniques into pipelines	Limieted scans are employed in comparison.	LIDC-IDRI	Acc – 0.9 Sens – 0.745 Spe – 0.9
[47]						
[48]	2020	ResUnet combined of Unet and ResNet34	Good results for VESSEL12, HUG-ILD, 24-LCTSC	Produced segmentation masks with lower quality for the CHUSJ private dataset.	VESSEL12 [52]	Dsc – 0.9778
					HUG-ILD [53]	
					24-LCTSC [54]	
					CHUSJ [48]	
[49]	2021	More than 40 pretrained baseline models	Data-efficient learning benchmark, and largest number of pretrained models	–	–	Dsc – 0.973 left lung Dsc – 0.977 right lung
[50]	2022	Improved UNET	Prevent the gradient instability, and effectively extract lung field characteristics	When the lung field is obscured by medical equipment, distorted, or substantially deformed from severe illnesses, the accuracy is comparatively low	JSRT [54]	Acc – 0.985, Spe – 0.985, Sen – 0.984, Dsc – 0.979, IoU – 0.958
					MC dataset [55]	Acc – 0.989, Spe – 0.993, Sen – 0.975, Dsc – 0.977, IoU – 0.955
[51]	2023	Nested UNET	First implementation of UNET++ for lung segmentation	–	MC dataset [55]	Acc – 0.98, IoU – 0.95
					Shenzhen Hospital X-ray [56]	

3 MATERIALS AND METHODS

3.1 Dataset

We use the CT Lung Nodule Analysis 2016 image dataset (LUNA 16) [57], which contains 888 3D thoracic CT scans and their masks, to train the reference models chosen for the comparison with our approach. This dataset is structured as follows: each CT scan has a couple of files, with the mhd/zraw extension, for the mask and another couple of files, with the mhd/raw extension, for the original images. We also use the Lung Image Database Consortium (LIDC) and the Image Database Resource Initiative (IDRI) [58], which contains 1018 three-dimensional images, including the 888 from LUNA16. We chose to utilize this database because it contains DICOM images whose metadata provide information necessary for our segmentation method, such as pixel spacing and slice thickness. We require LUNA for the masks, while the LIDC database is essential as it provides the individual images along with their metadata (slice position, slice thickness, pixel spacing ...).

3.2 Method

Our approach, as shown in Figure 1, consists of using the original images with pixel values in the range [–1000, +1000] HU (Hounsfield is the unit of measurement of the values obtained by the CT scanner) and increasing the resolution of the volume by additional interpolated images using the bicubic interpolation [59]. In addition, we use the region-growing algorithm only on pixels with values in the range [–1000, –500] HU, which corresponds to the region of interest, i.e., lung tissue and air. The automatically detected center of the optimal tracheal circle [13] will be used as a seed point to apply the region-growing to pre-segment the respiratory system (trachea + lungs).

The same point will also be used to segment the section of the trachea that lies outside the lungs; the region growing will be stopped before entering the lungs. Repair the lacunae due to blood vessels, trachea branches, and/or high-intensity lung damage using a combination of chain code and region growing. Ensure that the lungs are not connected by applying two times the region growing starting from the two extreme points at the left and right of the pre-segmented volume. If this is not the case, a separation process is required.

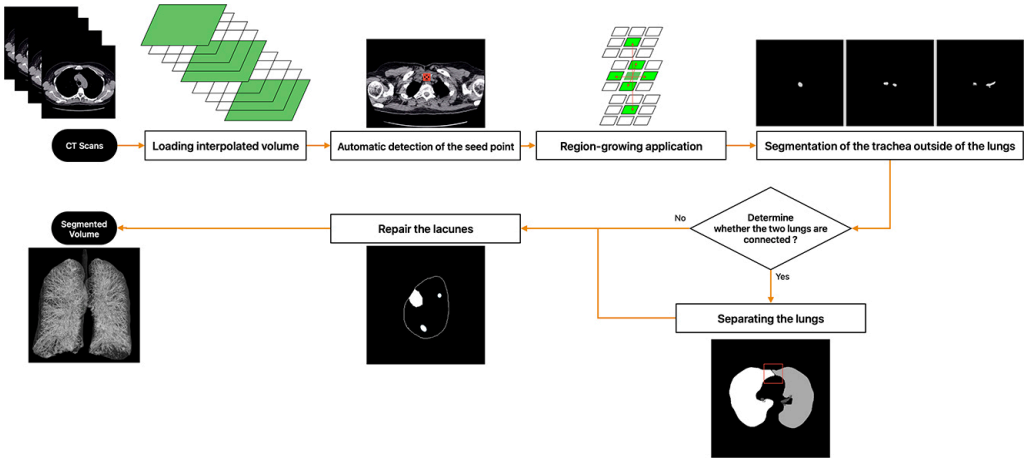

Fig. 1. Method flow chart

Loading interpolated volume. An image obtained by a CT scanner has a slice thickness and a square pixel size, which are determined by the scanner's sensor strip. To achieve higher resolution with more detailed information and improve volume quality, we considered adding interpolated images between each two successive images to finally obtain a cubic-shaped voxel, as shown in Figure 2.

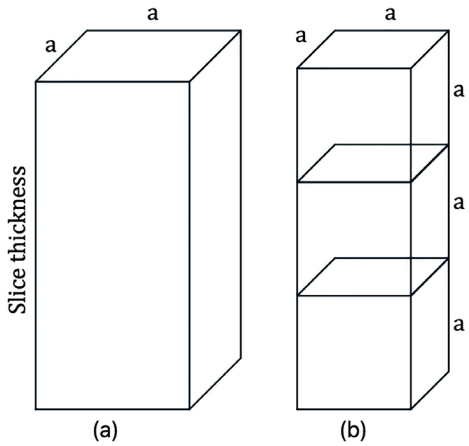

Fig. 2. (a) Original voxel shape form (b) Cubic shape form of the interpolated voxel

Due to the 3D bicubic interpolation, we observe the augmentation of the number of slices, which reflects the resolution increasing; consequently, the detail of the organs' shapes becomes increasingly closer to reality, which provides more information about the region we are interested in, as shown in Figure 3.

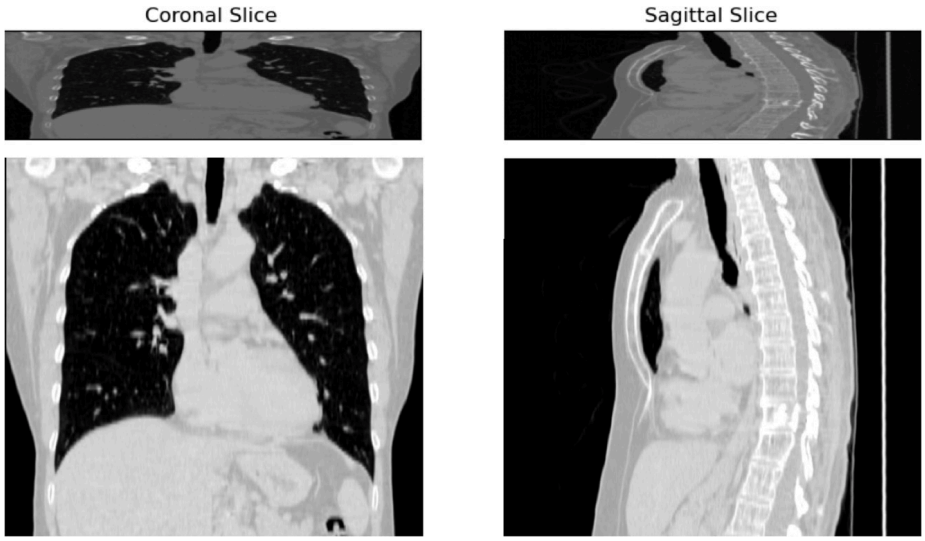

Fig. 3. Top: Without interpolation; Bottom: With interpolation

Principle of 3D bicubic interpolation: For a point $P(x, y, z)$ in 3D space, the interpolated value $I(x, y, z)$ is determined in a three-stage process:

1. Interpolation in the x dimension: For each Z_K plane, perform a cubic interpolation based on the 4 adjacent points along the x-axis.

$$I(x,y,z)=\sum_{i=-1}^{2} w_x(i).f(x_i,y,z) \quad (1)$$

2. Interpolation in the y dimension: For each plane X_i, use the intermediate results from the previous step to interpolate in the y direction.

$$I_y(z)=\sum_{j=-1}^{2} w_y(j).I_z(y_j,z) \quad (2)$$

3. Interpolation in the z dimension: Merge the interpolation results from the first two dimensions to perform an interpolation in the z dimension.

$$I(x,y,z)=\sum_{k=-1}^{2} w_z(k).I_y(z_k) \quad (3)$$

Automatic detection of the seed point. In the search frame, as shown in Figure 4a, limited by 100 pixels on each side of the image center. Each pixel found in the ROI interval ([–1000, –500] HU, as shown in Table 2) will be a seed point for applying a 2D region-growing to mark a region, to which we calculate parameters as described in our previous work [13], allowing us to detect regions that have some kind of circular shape, and each region will have a score. This process is repeated for each of the first twenty axial slices, and the region with the highest score will be the optimal tracheal circle, whose center will be our seed point, as shown in Figure 4b, for the 3D region-growing application.

Table 2. Some anatomical structure Housfield range [13]

	Bone	Liver	Muscle	Water	Lung	Air
Min (HU)	+1000	+40	+10	0	–700	–1000
Max (HU)	+1000	+60	+40	0	–500	–1000

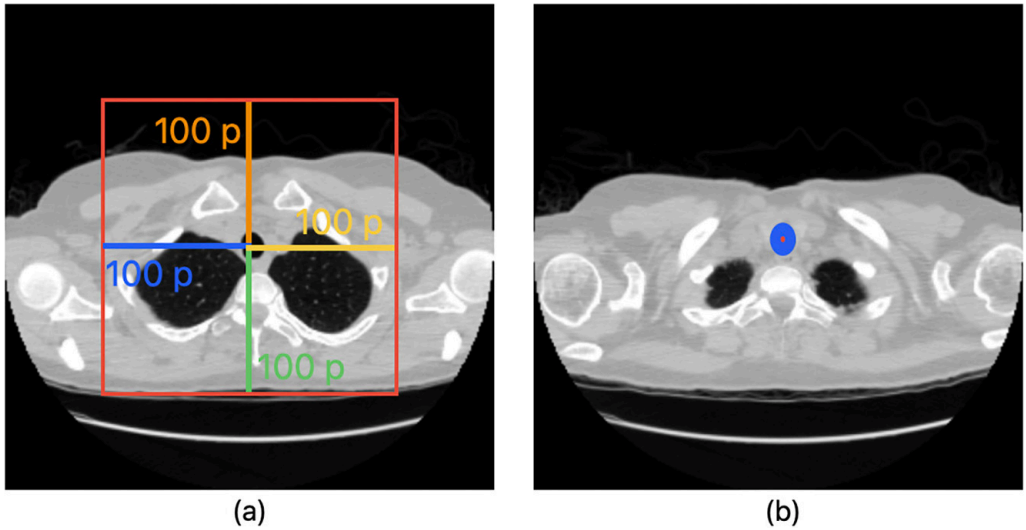

Fig. 4. (a) The search zone (b) The optimal tracheal circle

Region-growing application. To identify the pixels/voxels that are part of our area of interest, we apply the region-growing algorithm as follows:

1. Insert the seed point in a list.
2. Explore the neighbors.
   2.1. For 2D, a 4-connected neighborhood is used, while for 3D, a 6-connected neighborhood is used.
   2.2. Mark
      2.1.1. All pixels/voxels located in the range [–1000, –500] HU.
      2.2.2. For each pixel/voxel marked, we insert it into the list of seed points.
3. Delete the current point from the list.
4. Proceed in the same way for each point in the list.
5. Stop when there are no more points in the list.

At this stage, the application of 3D region-growing will segment the volume with gaps caused by blood vessels, tracheal branches, and/or lesions. A mechanism must therefore be put in place to correct these gaps. However, before applying the correction, we need to ensure that the lungs are not connected. To do this, the part of the trachea that lies outside the lungs must be labeled differently from the lungs.

Note that during the application of 3D region-growing, we will also identify,

- Rectangles delimiting our area of interest in each slice, recording the x, y coordinates of the two points located at opposite corners, as shown by the blue points in Figure 5a.
- Cube surrounding our volume of interest, recording the x, y, and z coordinates of the two opposite corners of the cube, the front point at top left and rear point at bottom right, as shown by the blue points in Figure 5b.

The purpose of this information is to limit the working area in the following steps.

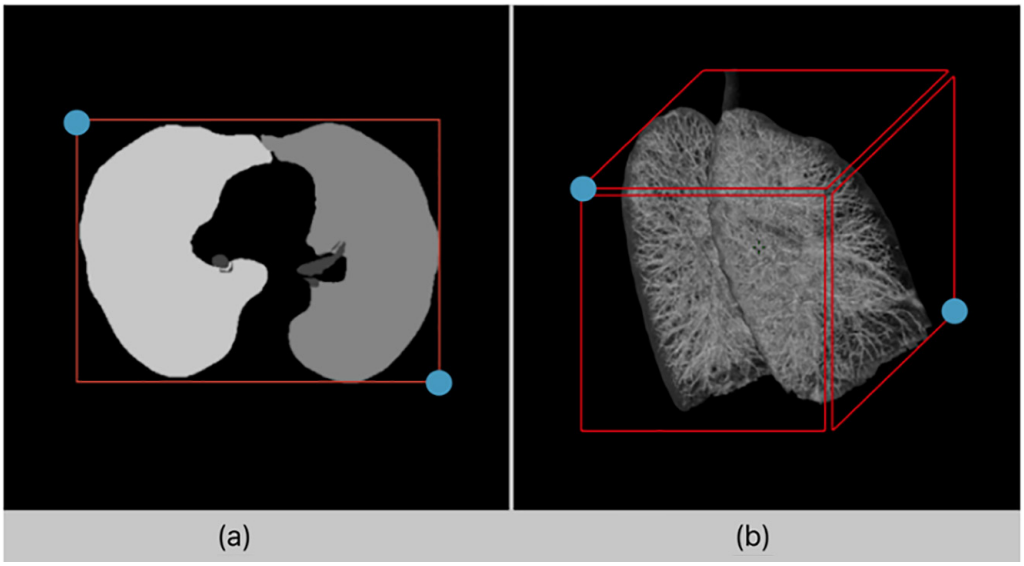

Fig. 5. (a) Rectangle delimiting ROI (b) Cube surrounding our VOI

Segmentation of the trachea outside the lungs. The aim is to segment the portion of the trachea located outside the lungs, knowing that the targeted volume is already included in the pre-segmented volume of the previous step. We take the initially detected seed point to apply 2D region growing for each slice to mark a region that must be connected to the region marked in the previous slice. The operation is

interrupted when the region surface in the current slice significantly exceeds the previous slices. As a result, Figure 6. shows the marked part of the trachea outside the lungs.

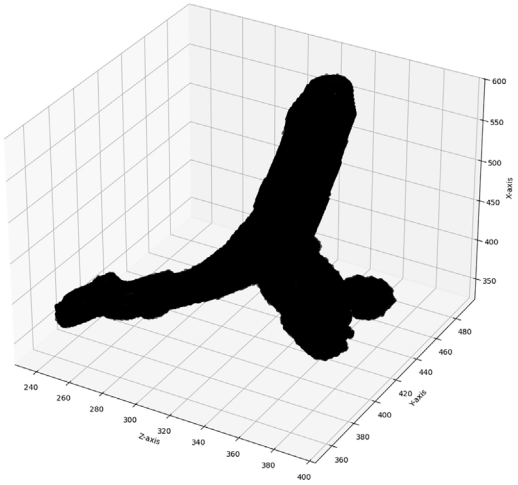

Fig. 6. Segmentation of the targeted volume of the trachea outside the lungs

Determine whether the two lungs are connected. Choose two points of contact between the volume of interest and the surrounding cube, on the right and left rectangular faces of the cube, as shown in Figure 7. Taking these two points into account, we apply a 3D region-growing. If we detect two volumes, this means that the two lungs are not connected. If they are, we start the separation process.

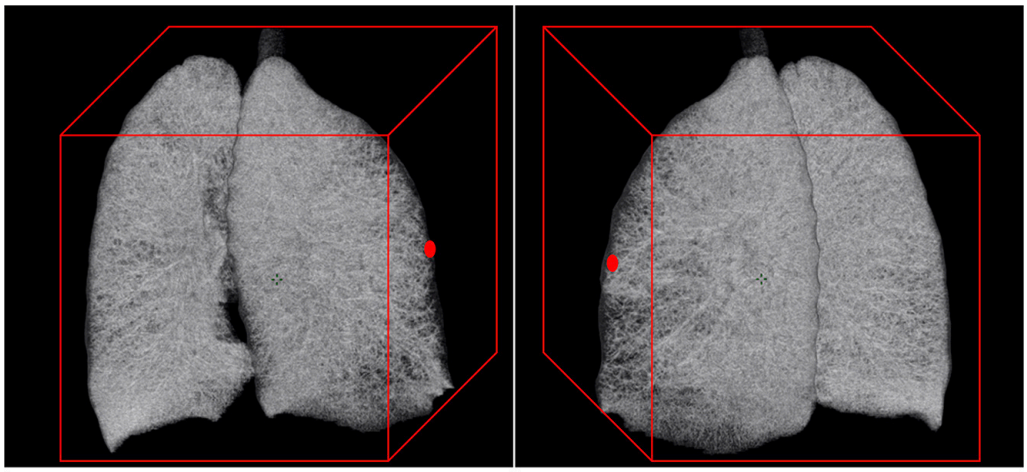

Fig. 7. (a) The right seed point (b) The left seed point

Separating the lungs. We will examine the separation of the lungs for each slice. At this stage, we have the rectangles delimiting our region of interest for each slice, as shown in Figure 8a. We divide the rectangle into three sub-rectangles of identical dimensions, as shown in Figure 8b, then apply 2D region growing to each sub-rectangle. This operation is performed successively on the right and left, using the pixels belonging to our ROI at the extremities of each sub-rectangle as seed points. The sub-rectangle containing a single region corresponds precisely to the contact location. In this sub-rectangle, we employ the combination of erosion to

remove contour labels and 2D region-growing as explained above until we obtain two labeled regions. Then, we start by applying dilation to identify the contours by the label of the adjacent region and remove the pixels that are in contact with both regions. In the end, we obtain a separated lung in the current slice, as shown in Figure 8c. After separation, a 3D region-growing is performed to label the volumes of the right and left lungs.

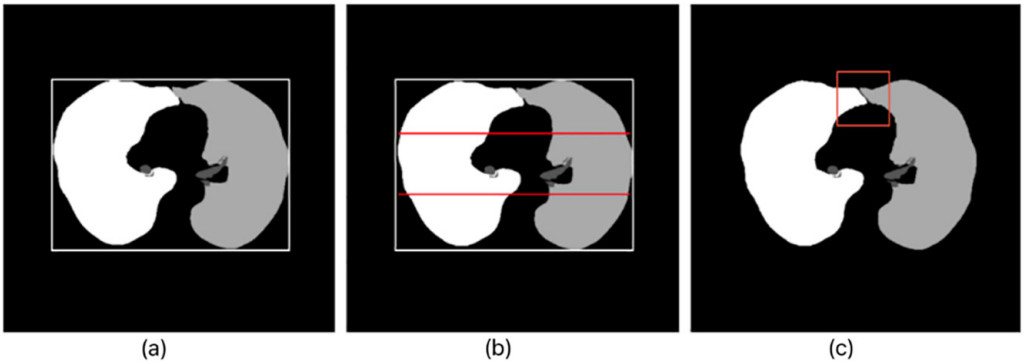

Fig. 8. (a) Rectangle delimiting a 2D ROI (b) Limit the contact search zone (c) Result of the separation

Repair the lacunes. Initially, we examine each slice to identify the chain code of the contours as illustrated in [60]. Based on this form information, we can identify openings to the outer surface of the lungs that create convexity, as shown in Figure 9a. Subsequently, we define the boundaries of this convexity as shown in Figure 9b. Finally, we draw a line and close these openings as shown in Figure 9c.

Next, we apply a 3D region-growing from the eight corners of the cube that surrounds the volume to identify the space outside our volume of interest. At this level, we mark the exterior and the voxels that are part of our segmented volume. However, the empty spaces remain unidentified. We perform a two-dimensional analysis, and when we find an unlabeled pixel, we use a 2D region-growing to label all the pixels in this region. At the end, we examine which lung this hole belongs to by identifying the lung that is in contact with the hole's contour and assigning its label to this hole. The process is repeated for the other holes.

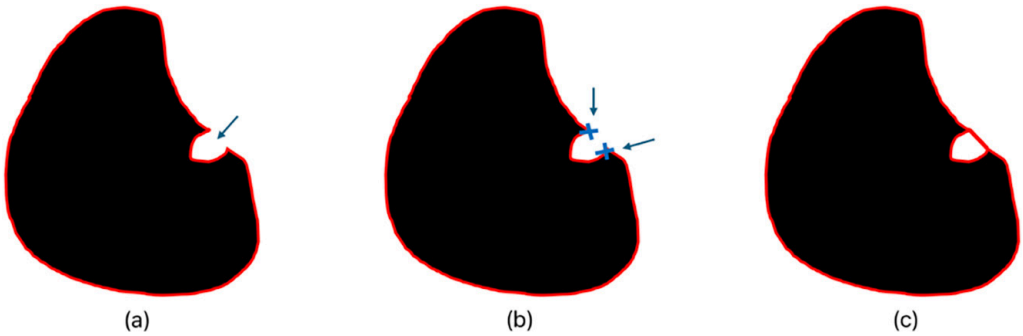

Fig. 9. (a) Opening hole (b) Convexity boundaries (c) Draw a line to close the opening hole

Figure 10 shows an example of the final segmentation result for the LIDC-IDRI-0002 CT scan.

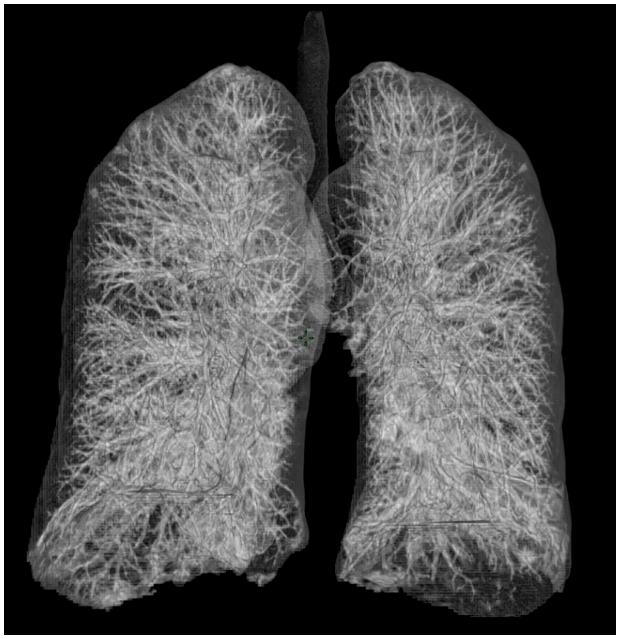

Fig. 10. Example of the final lung segmentation

3.3 Evaluation metrics

Ground truth validation [61] improves algorithms by identifying errors, ensures the reliability of results, particularly for important medical diagnoses, and provides a reliable benchmark for assessing performance.

Note:

TP = True Positive
TN = True Negative
FP = False Positive
FN = False Negative
Is = Segmented Image
Ig = Ground Truth Value

Statistical measurements: Accuracy, sensitivity, precision, and F-score are the metrics used to quantify and assess the image segmentation quality score.

- Accuracy is frequently used to characterize the segmentation performance of the model. On a scale of 0 to 100 percent, a higher value indicates better segmentation. It is calculated with this formula:

$$\frac{TP + TN}{TP + TN + FP + FN} \tag{4}$$

- Sensitivity, also known as recall, is used to measure the degree of accuracy of a favorable forecast. It is calculated with this formula:

$$\frac{TP}{TP + FN} \tag{5}$$

- Precision is used to determine the percentage of correct predictions using the predicted mask and the associated ground truth. It is calculated with this formula:

$$\frac{TP}{TP + FP} \tag{6}$$

- The F1-score is calculated with the following formula by taking the harmonic mean of the precision and recall values. Therefore, simultaneously optimizing precision and recall is necessary to maximize the F1 score:

$$\frac{2}{\frac{1}{Precision} + \frac{1}{Recall}} \tag{7}$$

Overlapping measures: These metrics, which also include widely used metrics like the Jaccard Index and the Dice Similarity, are used to find overlapping and non-overlapping regions in segmented images and ground truth.

- Dice similarity is used to assess the similarity of a predicted mask with its ground truth mask. A score of 1 indicates perfect overlap, while a score of 0 indicates no overlap. Calculated by the following formula,

$$\frac{2TP}{TP + FP + FN} \tag{8}$$

- The Jaccard index, also known as recall, is used to compare the predicted mask and the ground truth mask. Calculated by the following formula,

$$\frac{Is \cup Ig}{Is \cap Ig} \tag{9}$$

4 RESULTS AND DISCUSSION

This section covers the validation of our method using commonly used metrics, described in the next section, that guarantee the accuracy of segmentation and classification algorithms. We therefore decided to train the UNET, UNET++, and 3D-UNET models to segment the lung and take them as a reference for comparison with our proposed method.

4.1 Experimental results

a) Training: To ensure the credibility of our study, we are going to train the models chosen for comparison. To improve the accuracy of these models, we will target only pixels for 2D images and voxels for volume in our interval of interest between –1000 and –500 HU, as shown in Table 2. The training was run on the hardware accelerator A 100 GPU with 40 GB system RAM and 40 GB GPU RAM in Google Colab Pro. During the training phase, each model was trained volume by volume, which means it takes all the images from a volume before going to the next one. With the following parameters:

- Batch size: 8
- Epochs: 20
- Callback: model checkpoint, early stopping

These parameters were determined through experimentation on a reduced dataset prior to the final training in order to achieve the best results.

Of the 888 volumes in the LUNA 16 dataset, 728 are used for training, and 160 volumes are reserved for testing and validation.

Figure 11 shows the changes in different metric scores, for each model, during the training phase. As we can observe, for UNET and UNET++ the metrics reach stability from the 5th epoch. Instead of the 3D-UNET, reach stability around the 15th epoch.

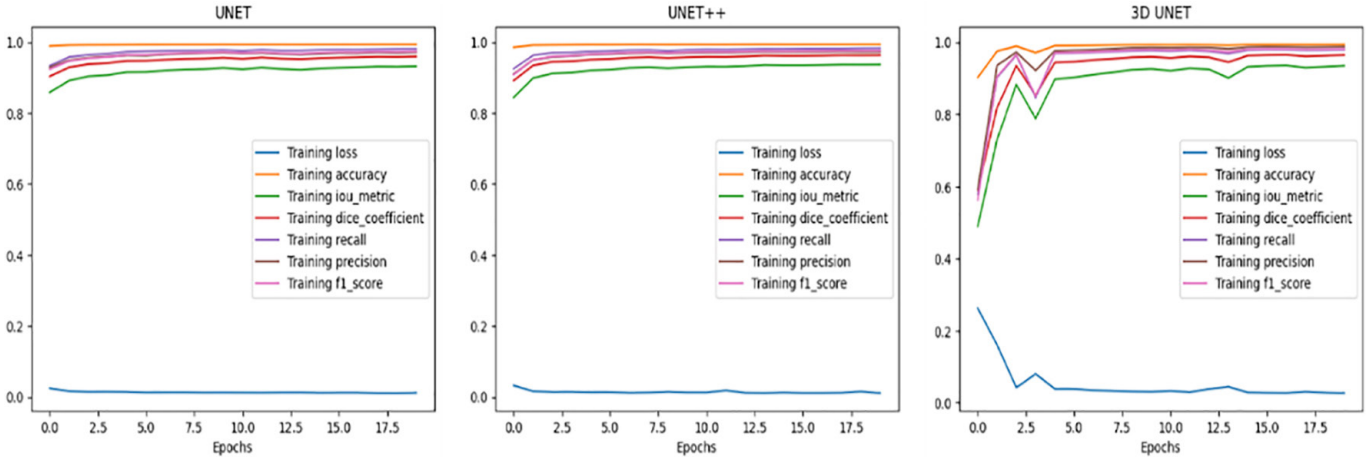

Fig. 11. Metric graph for UNET, UNET++, and 3D UNET during the training phase

b) Quantitative evaluation: To comprehensively evaluate the segmentation performance of the proposed method, we conducted extensive comparative experiments using the UNET, UNET++, and 3D-UNET models for lung segmentation. The results of the quantitative evaluation, based on validation metrics, obtained for the 160 patients from the LUNA 16 dataset are presented in Table 3.

Table 3. Performance metrics comparison

	UNET	UNET++	3D-UNET	OURS
Accuracy %	99.39	99.40	99.33	99.99
Jaccard Index %	94.29	95.27	95.97	97.96
Dice Similarity %	96.81	97.38	97.94	98.96
Recall %	98.47	98.57	99.23	98.38
Precision %	97.23	97.59	97.83	99.56
F1 score %	97.76	98.01	98.52	98.96

As seen, the performance of the proposed method was demonstrated by the accuracy value, which was very close to 100% within a difference of 0.01%. Thus, the method was able to improve the dice coefficient by 1.02–2.15%, reflecting how close we came to the ground truth mask. Similarly, other metrics were increased by 1.99–3.67% for the Jaccard index, 1.73–2.33% for precision, and 0.44–1.2% for the F1-score. Except for Recall, where our proposal was in last place with a minor difference of 0.09–0.85%. These results are clearly visible in Figure 12, which shows a graph for each metric for the 160 patients used for testing and validation.

Our method is represented by the red curve, which is practically positioned over the others with a visible margin. Except for the recall, which remains close to the others.

Fig. 12. Metric charts of the 160 CT volumes used for test and validation

In Table 4, we examined the time required for each model to perform training as well as the time needed to achieve 3D segmentation. The results show that the 3UNET model is the best in terms of response time after training, which lasted 9 hours and 23 minutes. However, our method presents significant competition, as it does not require training and remains close to the average segmentation time of the 3D-UNET model.

Table 4. Training time and time for 3D segmentation of the 160 volumes

	UNET	UNET++	3D-UNET	Our
Training	10h40m	18h37	9h23m	–
Segmentation min time	15.1 s	350 s	13.7 s	15.3 s
Segmentation max time	352.9 s	459.6 s	108.2 s	180.1 s
Segmentation avg time	193.6 s	280.3 s	**54.4 s**	68.1 s

c) Qualitative evaluation: To validate the effectiveness of our method, in this experiment, 7 patients were randomly selected for examination. The visualization results of the segmentation are shown in Figure 13. And because we added some interpolated images, we note the comparison is made only on the original slices.

As can be seen, the first 5 rows show that UNET, UNET++, and 3D-UNET fail to segment certain parts from the lungs, especially the part where there is contact between the lungs and the main trachea. In the remaining rows, UNET and 3D-UNET identify some parts of the colon. While our method identifes the lungs correctly, avoiding these errors.

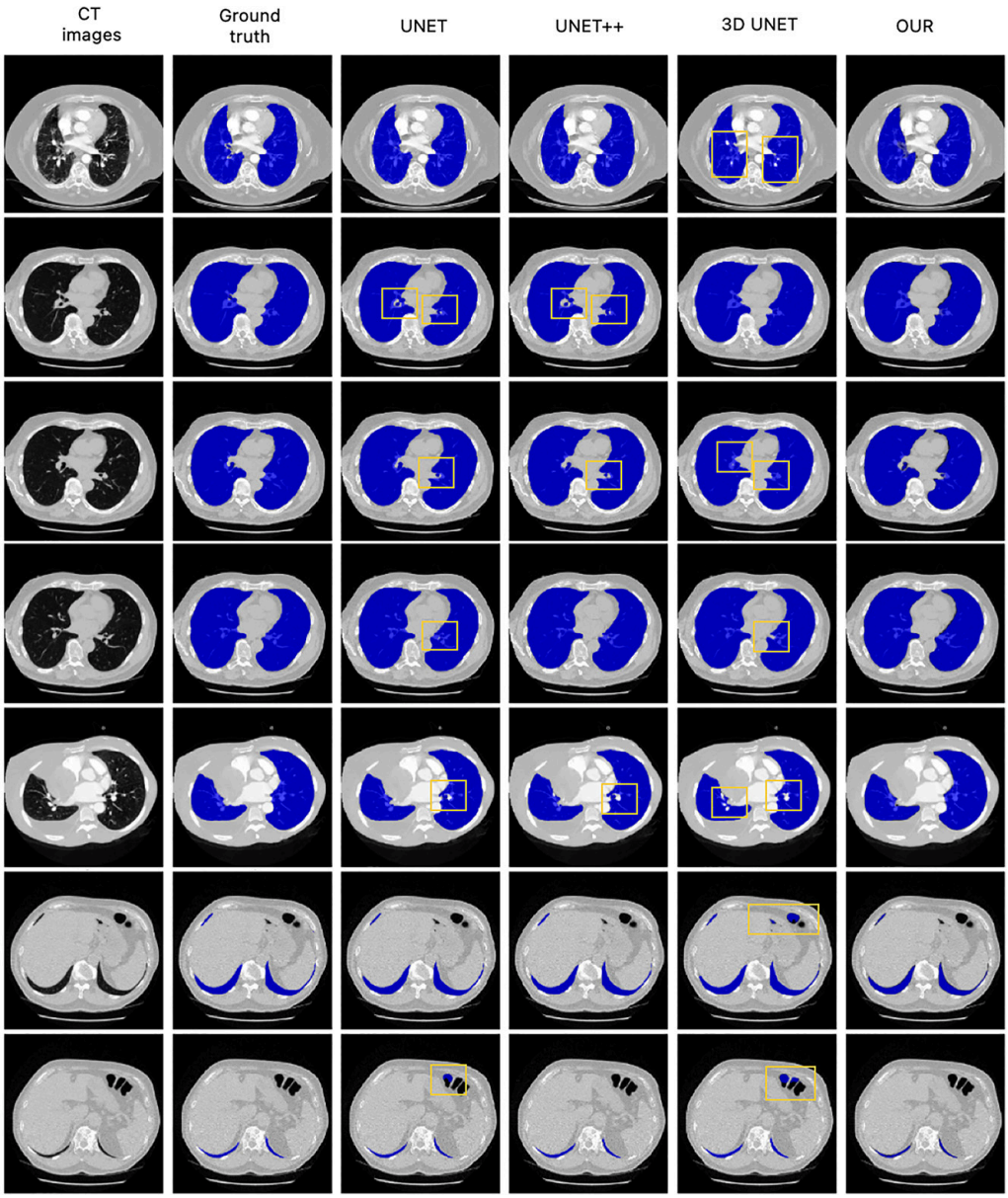

Fig. 13. Comparison of the ground truth to the outcomes of segmenting CT images using UNET, UNET++, 3D-UNET, and our segmented masks

5 CONCLUSION

This paper presents a novel approach for segmenting the respiratory system from a CT scan medical image based on increasing the volume resolution by using bicubic interpolation, which provides more details for the targeted organ structures; a region-growing algorithm to mark the volume starting from a seed point detected

automatically inside the trachea; and mathematical morphologies to repair the lacunae due to the parts that have high intensity.

As is known, the region-growing algorithm has some limitations. So, to overcome these limitations, we increased the volume resolution by adding new interpolated images to gain more textural information. We detected automatically the steep point inside the main trachea using the best circle algorithm. By restricting the working zone inside the cube and rectangles determined during the first round of the 3D region-growing application and taking into account only voxels that are in the range of –1000 and –500 HU, we were able to decrease the amount of time required to complete the task.

This method is tested against an artificial intelligence model based on convolutional neural networks, known as UNET, as well as its variants UNET++ and 3D-UNET. Based on validation metrics, we have demonstrated that the suggested approach offers extremely high segmentation accuracy.

The images, acquired by an X-ray scanner, have a thickness that reflects the distance between two successive images. In some cases, this thickness can reach up to 2.5 cm, depending on the acquisition configuration. However, our method is based on the pixel dimension in millimeters (generally around 0.474609375 mm). This implies that the greater the thickness, the greater the number of interpolated new images. In the case of 2.5 cm, approximately 52 interpolated images need to be created, which is simply not ideal for our method. This is noted as a perspective for future research.

6 REFERENCES

[1] "World Health Organization (WHO)." Consulté le: 10 février 2025. [En ligne]. Disponible sur: https://www.who.int

[2] D. F. Yankelevitz, R. Yip, and C. I. Henschke, "Impact of duration of diagnostic workup on prognosis for early lung cancer," *Journal of Thoracic Oncology*, vol. 18, no. 4, pp. 527–537, 2023. https://doi.org/10.1016/j.jtho.2022.12.020

[3] S. Kaneda *et al.*, "P1.16-02 three dimensional volumetric analysis is useful to improve diagnostic accuracy in early-stage lung adenocarcinoma," *Journal of Thoracic Oncology*, vol. 18, no. 11, p. S220, 2023. https://doi.org/10.1016/j.jtho.2023.09.358

[4] S. Machnicki *et al.*, "The usefulness of chest CT Imaging in patients with suspected or diagnosed COVID-19: A review of literature," *CHEST*, vol. 160, no. 2, pp. 652–670, 2021. https://doi.org/10.1016/j.chest.2021.04.004

[5] F. Baselice, G. Ferraioli, M. Ambrosanio, V. Pascazio, and G. Schirinzi, "Enhanced Wiener filter for ultrasound image restoration," *Computer Methods and Programs in Biomedicine*, vol. 153, pp. 71–81, 2018. https://doi.org/10.1016/j.cmpb.2017.10.006

[6] A. Khmag, "Additive Gaussian noise removal based on generative adversarial network model and semi-soft thresholding approach," *Multimed. Tools Appl.*, vol. 82, pp. 7757–7777, 2023. https://doi.org/10.1007/s11042-022-13569-6

[7] M. Sarkar and A. Mandal, "SLAAHE: Selective Apex Adaptive Histogram Equalization," *Franklin Open*, vol. 3, p. 100023, 2023. https://doi.org/10.1016/j.fraope.2023.100023

[8] S. B. Feinstein *et al.*, "Contrast enhanced ultrasound imaging," *Journal of Nuclear Cardiology*, vol. 17, no. 1, pp. 106–115, 2010. https://doi.org/10.1007/s12350-009-9165-y

[9] T. S. Deepthi Murthy and G. Sadashivappa, "Brain tumor segmentation using thresholding, morphological operations and extraction of features of tumor," in *2014 International Conference on Advances in Electronics Computers and Communications*, 2014, pp. 1–6. https://doi.org/10.1109/ICAECC.2014.7002427

[10] K. Siang Tan and N. A. Mat Isa, "Color image segmentation using histogram thresholding – Fuzzy C-means hybrid approach," *Pattern Recognition*, vol. 44, no. 1, pp. 1–15, 2011. https://doi.org/10.1016/j.patcog.2010.07.013

[11] F. Y. Shih and S. Cheng, "Automatic seeded region growing for color image segmentation," *Image and Vision Computing*, vol. 23, no. 10, pp. 877–886, 2005. https://doi.org/10.1016/j.imavis.2005.05.015

[12] Z. Yang, Y. Zhao, M. Liao, S. Di, and Y. Zeng, "Semi-automatic liver tumor segmentation with adaptive region growing and graph cuts," *Biomedical Signal Processing and Control*, vol. 68, p. 102670, 2021. https://doi.org/10.1016/j.bspc.2021.102670

[13] H. Hamza, B. Omar, A. A. Abdelkaher, and E. M. Abdelmajid, "Adaptive region growing based on detecting the seed point in the central trachea to the pre-segment respiratory system," in *2022 11th International Symposium on Signal, Image, Video and Communications (ISIVC)*, 2022, pp. 1–5. https://doi.org/10.1109/ISIVC54825.2022.9800747

[14] M. Sarkar and A. Mandal, "Follicle segmentation from ultrasound images of ovary by using sub-band entropy-based wavelet thresholding and object contours," in *2021 IEEE 18th India Council International Conference (INDICON)*, 2021, pp. 1–6. https://doi.org/10.1109/INDICON52576.2021.9691677

[15] Z.-F. Pang *et al.*, "Adaptive weighted curvature-based active contour for ultrasonic and 3T/5T MR image segmentation," *Signal Processing*, vol. 205, p. 108881, 2023. https://doi.org/10.1016/j.sigpro.2022.108881

[16] A. Abatal *et al.*, "Hybrid long short-term memory and decision tree model for optimizing patient volume predictions in emergency departments," *International Journal of Electrical and Computer Engineering (IJECE)*, vol. 15, no. 1, pp. 669–676, 2025. https://doi.org/10.11591/ijece.v15i1.pp669-676

[17] A. Abatal, M. Mzili, T. Mzili, K. Cherrat, A. Yassine, and L. Abualigah, "Intelligent interconnected healthcare system: Integrating IoT and big data for personalized patient care," *International Journal of Online and Biomedical Engineering (iJOE)*, vol. 20, no. 11, pp. 46–65, 2024. https://doi.org/10.3991/ijoe.v20i11.49893

[18] T. Mzili *et al.*, "Enhancing COVID-19 vaccination and medication distribution routing strategies in rural regions of Morocco: A comparative metaheuristics analysis," *Informatics in Medicine Unlocked*, vol. 46, p. 101467, 2024. https://doi.org/10.1016/j.imu.2024.101467

[19] B. Ait Skourt, A. El Hassani, and A. Majda, "Lung CT image segmentation using deep neural networks," *Procedia Computer Science*, vol. 127, pp. 109–113, 2018. https://doi.org/10.1016/j.procs.2018.01.104

[20] Y. Guo *et al.*, "A review of semantic segmentation using deep neural networks," *Int. J. Multimed. Info. Retr.*, vol. 7, pp. 87–93, 2018. https://doi.org/10.1007/s13735-017-0141-z

[21] Y. Lecun, L. Bottou, Y. Bengio, and P. Haffner, "Gradient-based learning applied to document recognition," *Proceedings of the IEEE*, vol. 86, no. 11, pp. 2278–2324, 1998. https://doi.org/10.1109/5.726791

[22] A. Krizhevsky, I. Sutskever, and G. E. Hinton, "ImageNet classification with deep convolutional neural networks," in *Advances in Neural Information Processing Systems*, *NeurIPS Proceedings*, 2012. https://proceedings.neurips.cc/paper_files/paper/2012/hash/c399862d3b9d6b76c8436e924a68c45b-Abstract.html

[23] C. Szegedy *et al.*, "Going deeper with convolutions," in *2015 IEEE Conference on Computer Vision and Pattern Recognition (CVPR)*, 2015, pp. 1–9. https://doi.org/10.1109/CVPR.2015.7298594

[24] K. Simonyan and A. Zisserman, "Very deep convolutional networks for large-scale image recognition," in *3rd International Conference on Learning Representations*, 2015. http://arxiv.org/abs/1409.1556

[25] Y. Zhu and S. Newsam, "DenseNet for dense flow," in *2017 IEEE International Conference on Image Processing (ICIP)*, 2017, pp. 790–794. https://doi.org/10.1109/ICIP.2017.8296389

[26] J. Ezeobiejesi and B. Bhanu, "Latent fingerprint image segmentation using deep neural network," in *Deep Learning for Biometrics, Advances in Computer Vision and Pattern Recognition*, B. Bhanu and A. Kumar, Éds., Springer, Cham, 2017, pp. 83–107. https://doi.org/10.1007/978-3-319-61657-5_4

[27] O. Ronneberger, P. Fischer, and T. Brox, "U-Net: Convolutional networks for biomedical image segmentation," *Medical Image Computing and Computer-Assisted Intervention – MICCAI 2015*, N. Navab, J. Hornegger, W. M. Wells, and A. F. Frangi, Eds., vol. 9351, 2015. https://doi.org/10.1007/978-3-319-24574-4_28

[28] Ö. Çiçek, A. Abdulkadir, S. S. Lienkamp, T. Brox, and O. Ronneberger, "3D U-Net: Learning dense volumetric segmentation from sparse annotation," *Medical Image Computing and Computer-Assisted Intervention – MICCAI 2016*, S. Ourselin, L. Joskowicz, M. R. Sabuncu, G. Unal, and W. Wells, Eds., vol. 9901, 2016. https://doi.org/10.1007/978-3-319-46723-8_49

[29] O. Oktay *et al.*, "Attention U-Net: Learning where to look for the pancreas," in *1st Conference on Medical Imaging with Deep Learning (MIDL 2018)*, Amsterdam, The Netherlands, 2022. https://openreview.net/pdf?id=Skft7cijM

[30] Z. Zhang, Q. Liu, and Y. Wang, "Road extraction by deep residual U-Net," *IEEE Geoscience and Remote Sensing Letters*, vol. 15, no. 5, pp. 749–753, 2018. https://doi.org/10.1109/LGRS.2018.2802944

[31] X. Li, H. Chen, X. Qi, Q. Dou, C.-W. Fu, and P.-A. Heng, "H-DenseUNet: Hybrid densely connected UNet for liver and tumor segmentation from CT volumes," *IEEE Transactions on Medical Imaging*, vol. 37, no. 12, pp. 2663–2674, 2018. https://doi.org/10.1109/TMI.2018.2845918

[32] Z. Zhou, M. M. Rahman Siddiquee, N. Tajbakhsh, and J. Liang, "UNet++: A nested U-Net architecture for medical image segmentation," in *Deep Learning in Medical Image Analysis and Multimodal Learning for Clinical Decision Support. DLMIA ML-CDS 2018*, in Lecture Notes in Computer Science, D. Stoyanov et al., Eds., 2018, vol. 11045. https://doi.org/10.1007/978-3-030-00889-5_1

[33] M. Z. Alom *et al.*, "Recurrent residual convolutional neural network based on U-Net (R2U-Net) for medical image segmentation," *ArXiv*, 2018. https://www.semanticscholar.org/paper/Recurrent-Residual-Convolutional-Neural-Network-on-Alom-Hasan/27c761258329eddb90b64d52679ff190cb4527b5

[34] J. Chen *et al.*, "TransUNet: Transformers make strong encoders for medical image segmentation," *arXiv preprint arXiv:2102.04306*, 2021.

[35] H. Huang *et al.*, "UNet 3+: A full-scale connected UNet for medical image segmentation," in *ICASSP 2020 – 2020 IEEE International Conference on Acoustics, Speech and Signal Processing (ICASSP)*, Barcelona, Spain, 2020, pp. 1055–1059. https://doi.org/10.1109/ICASSP40776.2020.9053405

[36] X. Liao, J. Zhao, C. Jiao, L. Lei, Y. Qiang, and Q. Cui, "A segmentation method for lung parenchyma image sequences based on superpixels and a self-generating neural forest," *PLoS ONE*, vol. 11, no. 8, p. e0160556, 2016. https://doi.org/10.1371/journal.pone.0160556

[37] P. G. Cavalcanti *et al.*, "Lung nodule segmentation in chest computed tomography using a novel background estimation method," *Quant. Imaging Med. Surg.*, vol. 6, no. 1, pp. 16–24, 2016. https://doi.org/10.3978/j.issn.2223-4292.2016.02.06

[38] N. He, X. Zhang, J. Zhao, H. Zhao, and Y. Qiang, "Pulmonary parenchyma segmentation in thin CT image sequences with spectral clustering and geodesic active contour model based on similarity," in *Proc. SPIE 10420, Ninth International Conference on Digital Image Processing (ICDIP 2017)*, 2017. https://doi.org/10.1117/12.2281942

[39] J. Cha, M. M. Farhangi, N. Dunlap, and A. A. Amini, "Segmentation and tracking of lung nodules via graph-cuts incorporating shape prior and motion from 4D CT," *Med. Phys.*, vol. 45, no. 1, pp. 297–306, 2018. https://doi.org/10.1002/mp.12690

[40] H. Chung, H. Ko, S. J. Jeon, K.-H. Yoon, and J. Lee, "Automatic lung segmentation with Juxta-Pleural nodule identification using active contour model and Bayesian approach," *IEEE Journal of Translational Engineering in Health and Medicine*, vol. 6, pp. 1–13, 2018. https://doi.org/10.1109/JTEHM.2018.2837901

[41] X. Xiao *et al.*, "An automated segmentation method for lung parenchyma image sequences based on fractal geometry and convex hull algorithm," *Applied Sciences*, vol. 8, no. 5, p. 832, 2018. https://doi.org/10.3390/app8050832

[42] J. Yun *et al.*, "Improvement of fully automated airway segmentation on volumetric computed tomographic images using a 2.5 dimensional convolutional neural net," *Medical Image Analysis*, vol. 51, pp. 13–20, 2019. https://doi.org/10.1016/j.media.2018.10.006

[43] M. Usman, B.-D. Lee, S.-S. Byon, S.-H. Kim, B. Lee, and Y.-G. Shin, "Volumetric lung nodule segmentation using adaptive ROI with multi-view residual learning," *Sci. Rep.*, vol. 10, p. 12839, 2020. https://doi.org/10.1038/s41598-020-69817-y

[44] R. Jenkin Suji, W. Wilfred Godfrey, and J. Dhar, "Border to border distance based method for detecting Juxta-Pleural nodules," in *Computer Vision and Image Processing (CVIP 2020), Communications in Computer and Information Science*, S. K. Singh, P. Roy, B. Raman, and P. Nagabhushan, Eds., 2021, vol. 1376. https://doi.org/10.1007/978-981-16-1086-8_22

[45] R. J. Suji, W. W. Godfrey, and J. Dhar, "Border to border distance based lung parenchyma segmentation including juxta-pleural nodules," *Multimed. Tools Appl.*, vol. 82, pp. 10421–10443, 2023. https://doi.org/10.1007/s11042-022-13660-y

[46] R. J. Suji, S. S. Bhadouria, J. Dhar, and W. W. Godfrey, "Optical flow based background subtraction method for lung nodule segmentation," in *Computer Vision and Image Processing (CVIP 2019)*, *Communication in Computer and Information Science*, N. Nain, S. K. Vipparthi, and B. Raman, Eds., 2020, vol. 1147. https://doi.org/10.1007/978-981-15-4015-8_23

[47] R. J. Suji *et al.*, "Optical flow methods for lung nodule segmentation on LIDC-IDRI images," *J. Digit. Imaging*, vol. 33, pp. 1306–1324, 2020. https://doi.org/10.1007/s10278-020-00346-w

[48] J. Sousa *et al.*, "Lung segmentation in CT images: A residual U-Net approach on a Cross-Cohort dataset," *Applied Sciences*, vol. 12, no. 4, p. 1959, 2022. https://doi.org/10.3390/app12041959

[49] J. Ma *et al.*, "Toward data-efficient learning: A benchmark for COVID-19 CT lung and infection segmentation," *Medical Physics*, vol. 48, no. 3, pp. 1197–1210, 2021. https://doi.org/10.1002/mp.14676

[50] W. Liu, J. Luo, Y. Yang, W. Wang, J. Deng, and L. Yu, "Automatic lung segmentation in chest X-ray images using improved U-Net," *Scientific Reports*, vol. 12, p. 8649, 2022. https://doi.org/10.1038/s41598-022-12743-y

[51] S. Gite, A. Mishra, and K. Kotecha, "Enhanced lung image segmentation using deep learning," *Neural Comput. and Applic.*, vol. 35, pp. 22839–22853, 2023. https://doi.org/10.1007/s00521-021-06719-8

[52] R. D. Rudyanto *et al.*, "Comparing algorithms for automated vessel segmentation in computed tomography scans of the lung: The VESSEL12 study," *Medical Image Analysis*, vol. 18, no. 7, pp. 1217–1232, 2014. https://doi.org/10.1016/j.media.2014.07.003

[53] J. Yang *et al.*, "Data from Lung CT segmentation challenge 2017 (LCTSC)," *The Cancer Imaging Archive*, 2017. https://www.cancerimagingarchive.net/collection/lctsc/

[54] A. Depeursinge, A. Vargas, A. Platon, A. Geissbuhler, P.-A. Poletti, and H. Müller, "Building a reference multimedia database for interstitial lung diseases," *Computerized Medical Imaging and Graphics*, vol. 36, no. 3, pp. 227–238, 2012. https://doi.org/10.1016/j.compmedimag.2011.07.003

[55] J. Shiraishi *et al.*, "Development of a digital image database for chest radiographs with and without a lung nodule: Receiver operating characteristic analysis of radiologists' detection of pulmonary nodules," *Am. J. Roentgenol.*, vol. 174, no. 1, pp. 71–74, 2000. https://doi.org/10.2214/ajr.174.1.1740071

[56] S. Jaeger, S. Candemir, S. Antani, Y.-X. J. Wáng, P.-X. Lu, and G. Thoma, "Two public chest X-ray datasets for computer-aided screening of pulmonary diseases," *Quantitative Imaging in Medicine and Surgery*, vol. 4, no. 6, pp. 475–477, 2014. https://doi.org/10.3978/j.issn.2223-4292.2014.11.20

[57] A. A. A. Setio *et al.*, "Validation, comparison, and combination of algorithms for automatic detection of pulmonary nodules in computed tomography images: The LUNA16 challenge," *Medical Image Analysis*, vol. 42, pp. 1–13, 2017. https://doi.org/10.1016/j.media.2017.06.015

[58] S. G. Armato *et al.*, "The lung image database consortium (LIDC) and image database resource initiative (IDRI): A completed reference database of lung nodules on CT scans," *Medical Physics*, vol. 38, no. 2, pp. 915–931, 2011. https://doi.org/10.1118/1.3528204

[59] A. Esmaeilzehi, M. O. Ahmad, and M. N. S. Swamy, "MuRNet: A deep recursive network for super resolution of bicubically interpolated images," *Signal Processing: Image Communication*, vol. 94, p. 116228, 2021. https://doi.org/10.1016/j.image.2021.116228

[60] Y. Wei, G. Shen, and J. Li, "A fully automatic method for lung parenchyma segmentation and repairing," *J. Digit. Imaging*, vol. 26, pp. 483–495, 2013. https://doi.org/10.1007/s10278-012-9528-9

[61] N. Swathi and K. Sakthidasan Sankaran, "Advances and clinical implications of neuroanatomical biomarkers in schizophrenia by optimizing brain tissue segmentation," *Biomedical Signal Processing and Control*, vol. 102, p. 107215, 2025. https://doi.org/10.1016/j.bspc.2024.107215

7 AUTHORS

Hamza Halim is a software engineer and Ph.D. candidate in the Computer Science Department of the University of Chouaib Doukkali, Faculty of Sciences El Jadida in Morocco. He received a master's degree in "Intelligence system and networks" from Sidi Mohamed Ben Abdellah University, Fes. His research interests include medical image processing and artificial intelligence (E-mail: hamza.h@ucd.ac.ma).

Dr. Salma Hakim is a doctor and researcher in the Department of Computer Science at Chouaib Doukkali University, specializing in medical image processing and artificial intelligence (E-mail: hakim.s@ucd.ac.ma).

Dr. Omar Boutkhoum is a professor at the Faculty of Sciences El Jadida in Morocco and a member of the LAROSERI Laboratory. His research interests include "Theory of computation, Computer engineering, and Information systems" (E-mail: boutkoum.o@ucd.ac.ma).

Dr. Mohamed Hanine is a professor at National School of Applied Science in El Jadida, Morocco, and a member of the LTI Laboratory. His research interests include BI, Big data, MCDM (E-mail: m.hanine@uca.ma).

Dr. Abdelmajid El Moutaouakil is a professor at the Faculty of Sciences El Jadida in Morocco and a member of the LAROSERI Laboratory. His research interests include medical image processing and artificial intelligence (E-mail: elmou01@yahoo.com).